Journal of Power Sources 274 (2015) 1254–1262

Contents lists available at ScienceDirect

Journal of Power Sources

journal homepage: www.elsevier.com/locate/jpowsour

Surface chemistry of $LiNi_{0.5}Mn_{1.5}O_4$ particles coated by Al_2O_3 using atomic layer deposition for lithium-ion batteries

Jin Wook Kim [a], Dong Hyeon Kim [a], Dae Yang Oh [a], Hyeyoun Lee [b], Ji Hyun Kim [b], Jae Hyun Lee [b], Yoon Seok Jung [a, *]

[a] School of Energy and Chemical Engineering, Department of Energy Engineering, Ulsan National Institute of Science and Technology (UNIST), Ulsan 689-798, Republic of Korea
[b] Batteries R&D, LG Chem, Yusong-gu, Daejeon 305-380, Republic of Korea

HIGHLIGHTS

- Ultrathin (<1 nm) Al_2O_3 ALD film was deposited on $LiNi_{0.5}Mn_{1.5}O_4$ (LNMO) particles.
- Coulombic efficiency, cycleability, and self-discharge were improved by ALD.
- Thinner SEI layer with less organic components was observed for ALD coated LNMO.
- Fluorination of the Al_2O_3 ALD coating layer upon charge–discharge cycles was found.
- This fluorination accounts for the increasing capacities upon cycles.

GRAPHICAL ABSTRACT

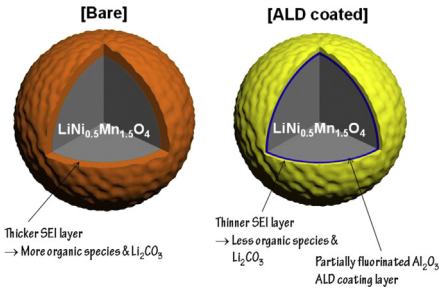

ARTICLE INFO

Article history:
Received 26 September 2014
Accepted 31 October 2014
Available online 1 November 2014

Keywords:
Battery
Lithium
Electrode
Cathode
Coating
Surface

ABSTRACT

The effects of depositing ultrathin (<1 nm) Al_2O_3 coatings on $LiNi_{0.5}Mn_{1.5}O_4$ (LNMO) particles using atomic layer deposition (ALD) are presented. Promising electrochemical performance of the Al_2O_3 ALD coated LNMO at 30 °C is demonstrated in not only significantly improved coulombic efficiency, cycle retention, and rate capability, but also in dramatically suppressed self-discharge and dissolution of transition metals. Combined analyses by electrochemical impedance spectroscopy, *ex-situ* X-ray photoelectron spectroscopy, and *ex-situ* time-of-flight secondary ion mass spectrometry reveal that the solid electrolyte interphase layer on the Al_2O_3 ALD coated LNMO is much thinner and contains fewer organic species than the one on the bare LNMO. This difference originates from the suppression of the side reaction at high voltage by the Al_2O_3 ALD protective coating. Also, fluorination of Al_2O_3 ALD layer upon repeated charge–discharge cycling is confirmed, and this can account for the capacity increases during the initial charge–discharge cycles. Finally, it is also demonstrated that a full LNMO/$Li_4Ti_5O_{12}$ battery incorporating the Al_2O_3 ALD coated LNMO outperforms the one incorporating only bare LNMO.

1. Introduction

By virtue of their high energy density, lithium-ion batteries (LIBs) are used as the power sources in most portable electronic devices [1,2]. Of late, LIBs have opened up new opportunities for

* Corresponding author.
E-mail address: ysjung@unist.ac.kr (Y.S. Jung).

http://dx.doi.org/10.1016/j.jpowsour.2014.10.207
0378-7753/

energy storage in large-format technologies including electric vehicles and smart grids [1,2]. With these applications in mind, several characteristics such as energy, safety, and cost need to be improved [1,2]. High energy densities in LIBs can be achieved by increasing either the capacity or the voltage. Efforts to develop high-capacity anode materials, such as silicon [3], and high-capacity cathode materials, such as sulfur [4] (theoretically, 1675 mA h g^{-1}) and Li-excess transition metal oxides [5] (Li[Li,Ni,Co,Mn]O_2, typically 200–250 mA h g^{-1}), are in line with the capacity-based approach to increase the energy density. Regarding the voltage: there is little room for further decreasing the voltage of the anode materials because conventional graphite already operates close to 0 V (*vs.* Li/Li^+) and silicon reacts with Li at low voltages [0.2–0.3 V (*vs.* Li/Li^+)]. Therefore, development of high-voltage cathode materials is the only one way to increase the overall voltage of batteries.

Spinel $LiNi_{0.5}Mn_{1.5}O_4$ (LNMO) is an attractive cathode material because it can operate at higher voltages [~4.7 V (*vs.* Li/Li^+)] than conventional $LiCoO_2$ [6–9]. Additionally, the energy density of LNMO (650 W h kg^{-1}) is ~20% higher than that of conventional $LiCoO_2$ [10]. The presence of three-dimensional diffusion channels for Li^+ ions in the spinel structure is an additional advantage of LNMO. Ni in LNMO exists as Ni^{2+} and is oxidized to Ni^{4+} upon Li^+ intercalation/extraction, while Mn^{4+} remains unchanged [8,9]. This feature prevents structural degradation by disproportionation reactions and Jahn-Teller distortion, both of which are associated with Mn^{3+} [8,11]. However, the fact that the high energy density of LNMO, enabled by the high operating voltage, is offset by limitations in the thermodynamic-stability window of conventional organic liquid electrolytes remains a critical issue [9,11]. Mn dissolution is also a serious problem, not only in $LiMn_2O_4$ but also LNMO [8,9,12]. The dissolved Mn^{2+} moves toward the anode and disrupts the solid electrolyte interphase (SEI) on the anode, resulting in rapid degradation of the full cells [13–15]. The stability of the electrode-electrolyte interface for LNMO at high voltages can be improved by either developing advanced electrolytes [16] or shielding the bare LNMO with coating materials [15,17,18].

Atomic layer deposition (ALD) is an attractive thin film deposition technique based on a sequential and self-limiting surface reaction [19]. Compared to the conventional wet methods [20], ALD offers several advantages such as excellent conformality and atomic-scale thickness control [21,22]. Also, because ALD offers relatively low operating temperatures [19], reactions between the substrate and the coating materials is not an issue in most cases. To date, Al_2O_3 ALD coatings deposited on various cathode materials including $LiCoO_2$ [21,23–25], Li[Ni,Co,Mn]O_2 [26,27], and Li-excess materials (Li[Li,Ni,Co,Mn]O_2) [28] and anode materials including graphite [7,22,25], silicon [29], and metal oxides [30,31] have been demonstrated to significantly improve the performance and safety of the cells. Recently, Al_2O_3 and $LiAlO_2$ ALD coatings deposited on as-formed LNMO composite electrodes have also been reported [15,18,32]. However, detailed and in-depth analyses of the behaviors of the ALD-modified LNMO are lacking. Especially, effect of the ALD coatings on surface chemistry of LNMO is yet unknown.

In this report, ultrathin (<1 nm) Al_2O_3 ALD coatings were deposited on LNMO particles. The effects of the Al_2O_3 ALD coating on the electrochemical performance of electrodes fabricated using these materials were examined. The coulombic efficiency, cycle retention, rate capability, self-discharge behavior, and dissolution of transition metals were enhanced. The relationship between the electrochemical performance and the features of the SEI, such as thickness and composition, for the Al_2O_3 ALD coated LNMO and the bare LNMO materials was investigated.

2. Experimental

2.1. Atomic layer deposition of Al_2O_3 on $LiNi_{0.5}Mn_{1.5}O_4$ powders

Al_2O_3 films were grown by ALD on $LiNi_{0.5}Mn_{1.5}O_4$ powders using a custom-made rotary ALD reactor, as described in previous reports [21,22]. The ALD precursors were trimethylaluminum (TMA) and H_2O. During ALD, a porous stainless-steel cylinder containing the powders in the reaction chamber rotated at 140 rpm. A single cycle of Al_2O_3 ALD sequence was: (1) dose with TMA to 1.0 Torr, (2) wait for the duration of TMA reaction, (3) evacuate chamber to eliminate reaction products (CH_4) and excess TMA, (4) dose with Ar to 20.0 Torr, (5) Ar static time, (6) evacuate chamber to purge Ar and any entrained gases; (7) dose with H_2O to 1.0 Torr, (8) wait for the duration of the H_2O reaction, (9) evacuate chamber to eliminate reaction products (CH_4) and excess H_2O, (10) dose with Ar to 20.0 Torr, (11) Ar static time, and (12) evacuate chamber to purge Ar and any entrained gases. ALD was conducted at 180 °C.

2.2. Materials characterization

X-ray diffraction (XRD) measurements were performed using a D8-Bruker Advance diffractometer with Cu K_α radiation (1.54056 Å). The Al content of the Al_2O_3 ALD coated LNMO powders was determined using inductively coupled plasma optical emission spectrometry (ICPOES, 720-ES, Varian). Field emission scanning electron microscopy (FESEM) images were obtained using a Nanonova 230 microscope (FEI). High-resolution transmission electron microscopy (HRTEM) images were obtained using a JEM-2100F microscope (JEOL).

2.3. Electrochemical characterization

The LNMO composite electrode was prepared by spreading the LNMO powder (Mitsui Corp.), Super P, and poly(vinylidene fluoride) (PVDF) binder (KF1100, Kureha Inc.) on a piece of Al foil in a weight ratio of LNMO:Super P:PVDF = 90:5:5. The mass of LNMO loaded into the composite electrode was ~5.5 mg cm^{-2}. 2032-type coin cells were assembled in an Ar-filled dry glove box. Galvanostatic charge–discharge cycling was performed over the potential window 3.0–5.0 V (*vs.* Li/Li^+) at 30 °C at a current density of 0.1C (14 mA g^{-1}) for the first two cycles and 0.5C for the subsequent cycles. Li metal foil was used as the counter electrode in the half cells. A 1.0 M solution of $LiPF_6$ dissolved in a mixture of ethylene carbonate (EC), ethyl methyl carbonate (EMC), and dimethyl carbonate (DMC) (3:4:3 v/v) (Panax Inc.) was used as the electrolyte. A porous polypropylene (PP)/polyethylene (PE)/PP tri-layer film (Celgard Inc.) was used as the separator. AC impedance measurements were performed using a signal with amplitude 10 mV over a frequency range from 100 kHz to 5 mHz using an IviumStat (IVIUM Technology Corp.). After the LNMO/Li half cells were discharged to 60 mA h g^{-1} at 0.1C after the requisite number of cycles and rested for 6 h, AC impedance spectra were recorded at the open circuit voltage, which was ~4.7 V (*vs.* Li/Li^+). For the full-cell tests, $Li_4Ti_5O_{12}$ (LTO) was used as the anode material. The composite anode included LTO, Super P, and PVDF (80:10:10 by weight). The mass ratio of LNMO/LTO in the LNMO/LTO full cells was ~1.4. The full cells of LNMO/LTO were cycled between 2.00 and 3.45 V at 0.5C. Based on the reversible capacities obtained from the half-cell experiments on LTO/Li (~160 mA h g^{-1} at 0.1C between 1.2 and 2.0 V), the np ratio of LNMO/LTO was determined to be ~0.9. All of the cells were assembled in an Ar-filled dry box and tested at 30 °C.

2.4. Ex-situ analyses

For the *ex-situ* analyses of the electrodes, the cycled electrodes collected from the disassembled coin cells were rinsed with

anhydrous DMC and dried in the Ar-filled dry box. For the *ex-situ* XRD analyses, a specially designed cell was used: the air-sensitive cycled electrodes were placed on a beryllium window and hermetically sealed inside the Ar-filled dry box. The amount of dissolved transition metal was obtained by the following procedure: The dissolved transition metals in the composite electrodes and the electrolytes were collected by rinsing the composite electrode, the separator, and the coin cell components in DMC. The transition metals deposited on the lithium metal counter electrode were collected by dissolving the cycled lithium metal in deionized water. (Caution: The reaction between lithium and water is dangerous.) The total amount of dissolved transition metals was determined using the aforementioned DMC and water solutions by ICPOES measurements. *Ex-situ* characterization with XPS was performed using a K-alpha X-ray photoelectron spectrometer (Thermo Fisher) with a monochromatic Al K_α source (1486.6 eV). Time-of-flight secondary ion mass spectrometry (TOFSIMS) analyses were conducted on a TOF SIMS 5 (ION TOF). A 25 kV Bi^+ and O^+ source was employed for analysis and sputtering. For the *ex-situ* XPS and TOFSIMS analyses, the LNMO/Li cells were discharged to 3.0 V at 0.1C after the selected cycle.

3. Results and discussion

The XRD patterns of the bare and Al_2O_3 ALD coated LNMO particles shown in Fig. 1a match well with a disordered phase with a space group of Fd^3m [7]. The XRD pattern of the Al_2O_3-coated LNMO is identical to that of the bare LNMO; this indicated that the ALD operation did not affect the bulk structure of LNMO. Fig. 1b and c show HRTEM images of the bare LNMO particles and the Al_2O_3-coated LNMO particles after 10 ALD cycles. It is apparent that a ~2-nm-thick amorphous layer was deposited on the crystalline substrate in Fig. 1c, a situation that is supported by previous reports in which the Al_2O_3 grown by ALD is amorphous and the ALD film growth rate on powders is ~2 Å per cycle [21]. As an alternative method to estimate the thickness of the Al_2O_3 ALD coating, the Al content of the Al_2O_3-coated LNMO particles was measured by ICPOES after 10 ALD cycles, giving 828 ppm. Given the surface area (0.25 m^2 g^{-1}) of LNMO as determined by the N_2 adsorption–desorption isotherm method and the specific density of ALD-grown Al_2O_3 (3.0 g cm^{-3}) [19], the thickness of the Al_2O_3 ALD film was calculated as 2.1 nm. This value agrees perfectly with the results in Fig. 1c and the calculation based on a growth rate of 2 Å per ALD cycle, demonstrating that the Al_2O_3 ALD coating on the LNMO is very conformal.

Fig. 2a shows the initial charge–discharge voltage profiles of bare and Al_2O_3 ALD coated LNMO at 0.1C (14 mA g^{-1}) at 30 °C. The plateaus at ~4 and ~4.7 V are associated with Mn^{3+}/Mn^{4+} and Ni^{2+}/Ni^{4+} redox reactions, respectively [8,9]. The occurrence of a plateau at 4 V is typical of a disordered phase [7–9]. Polarization increases with an increasing number of ALD cycles; consequently, the capacity decreases. Fig. 2b shows the discharge capacities at 0.1C and 0.5C as a function of the number of ALD cycles. The abrupt capacity decrease at 6 ALD cycles is associated with the impeded transport of both electrons and Li^+ ions through the insulating Al_2O_3 ALD coating layers, which agrees well with previous reports [21,22].

Fig. 2c depicts the cycle performances of bare and Al_2O_3 ALD coated LNMO cells cycled at 30 °C at 0.1C for the first two cycles and 0.5C for the subsequent cycles. The capacities of the LNMO electrodes subjected to 4, 6, and 10 ALD cycles increase with the number of charge/discharge cycles. The increases in capacity of the LNMO electrodes after the initial charge/discharge cycles are exceptionally large for the materials fabricated using 4 and 6 ALD cycles (indicated by the arrows). These increases may reflect gradual changes in the Al_2O_3 ALD coating layer, a possibility which

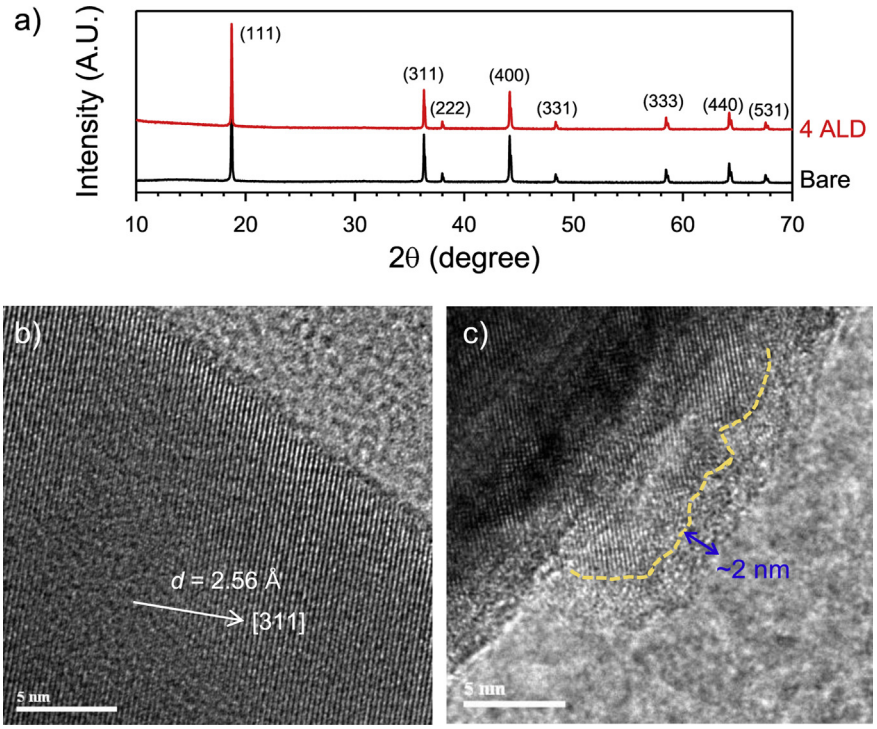

Fig. 1. a) XRD patterns of the bare and Al_2O_3 ALD coated (4 ALD cycles) LNMO powders. HRTEM images of b) the bare LNMO particles and c) the Al_2O_3 ALD coated (10 ALD cycles) LNMO particles.

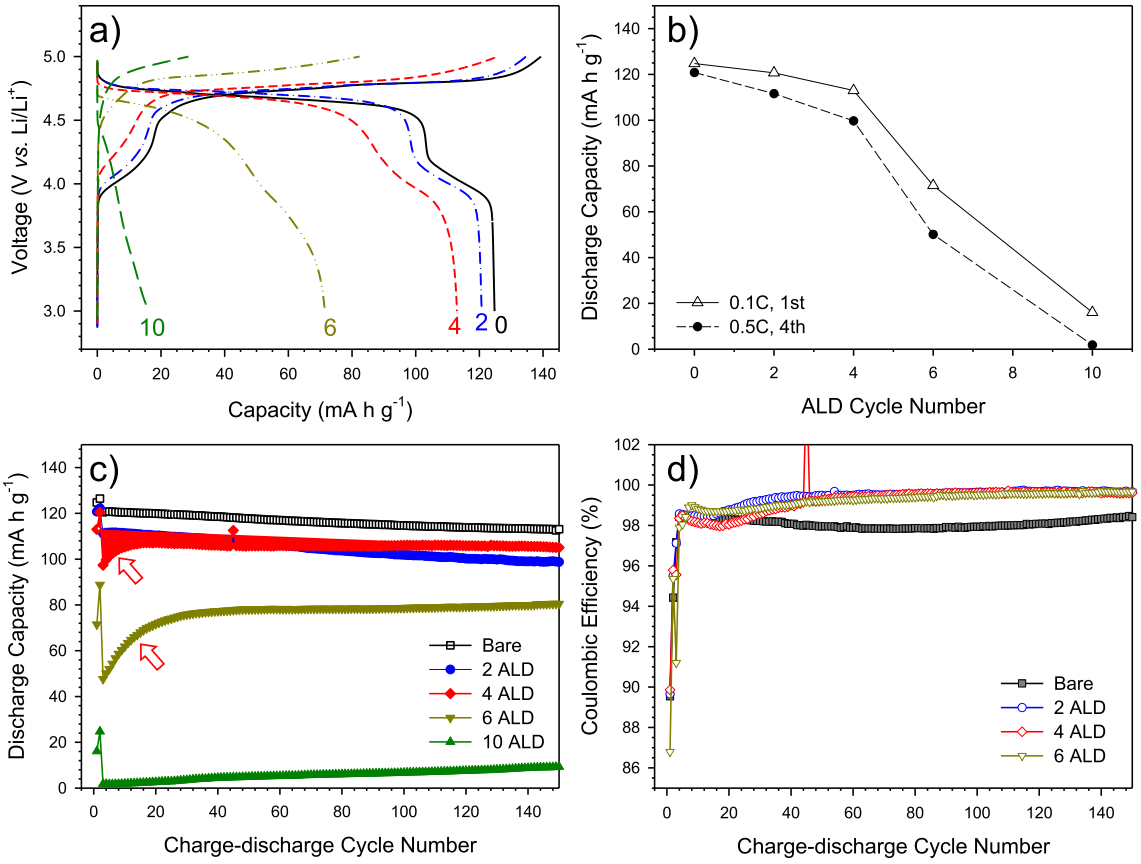

Fig. 2. a) Initial charge–discharge voltage profiles, b) discharge capacity as a function of ALD cycle number, c) cycle performance, and d) coulombic efficiency of the bare and Al_2O_3 ALD coated LNMO electrodes. The numerals in (a) indicate the ALD cycle numbers for each sample.

will be discussed in detail later. The 4 ALD cycles on LNMO show a significant improvement in capacity retention, while the 2 ALD cycles do not. If the capacity retention after the 150th charge–discharge cycle is compared to the retention after the 20th cycle (where the capacity stabilized), the LNMO with 4 ALD cycles exhibits a value of 98.0% while the bare LNMO gives 94.3%. Fig. 2d shows the coulombic efficiency of the bare and Al_2O_3 ALD coated LNMO electrodes. The coulombic efficiency is very important because it reflects the performance of the full cell, in which the Li source is limited [24]. For example, a coulombic efficiency of 99% indicates that the full battery loses 1.0% of its capacity every charge–discharge cycle, even if the half cell shows no capacity loss. No enhancement in coulombic efficiency by the Al_2O_3 coatings during the initial charge/discharge cycle is observed in Fig. 2d. However, at higher numbers of charge–discharge cycles, all the Al_2O_3 ALD coated LNMO electrodes exhibit much higher coulombic efficiencies than the bare LNMO electrodes do. For example, the coulombic efficiency of the coated LNMO after 4 ALD cycles at after the 80th charge–discharge cycle is 99.5%, which contrasted sharply with the value of 97.9% determined for the bare LNMO. Because the LNMO particles subjected to 4 ALD cycles showed optimal performance in terms of capacity, coulombic efficiency, and cycle performance, this material will be extensively compared to the bare LNMO in the following results.

Fig. 3 compares the rate performances of bare and Al_2O_3 ALD coated (using 4 ALD cycles) LNMO. Increasing the C-rate gradually from 0.1C to 2C resulted in slightly higher polarization and lower capacities in the Al_2O_3 ALD coated LNMO than in the bare LNMO. After prolonged charge–discharge cycling at 4C, however, the trend reversed. This behavior could have originated from severe degradation of the bare LNMO during charge–discharge cycling. The subsequent cycling at 1C starting from the 28th charge–discharge cycle results in noticeable difference in capacity fade between bare and Al_2O_3 ALD coated LNMO, indicating that accumulated fatigue produced by the side reactions at high C-rates is much more significant for the bare LNMO than the Al_2O_3 ALD coated material.

To compare changes in the resistances of bare and Al_2O_3 ALD coated (using 4 ALD cycles) LNMO, electrochemical impedance spectroscopy (EIS) measurements were conducted, as shown in Fig. 4. Fig. 4a shows Nyquist plots collected after different numbers of charge–discharge cycles. All spectra are comprised of two semicircles and a low-frequency tail. The high-frequency semicircle is associated with transport of Li^+ ions through the SEI film [33] or the inter-particle contact resistance in the composite electrodes [34]. The mid-frequency semicircle reflects the charge-transfer resistance at the electrode/electrolyte interface [33,35]. The low-frequency tail arises from Li^+ ion diffusion in the bulk LNMO [33,35]. After the spectra in Fig. 4a were fitted using the Randles circuit, as shown in Fig. 4b [35], the resistance values were obtained; these are plotted in Fig. 4c. Both the R_1 and R_2 values after the 2nd charge–discharge cycle for the Al_2O_3 ALD coated LNMO are higher than those for the bare LNMO, indicating that the transport of Li^+ ions was impeded by the insulating Al_2O_3 film. It should be emphasized that both the R_1 and R_2 values for the Al_2O_3 ALD coated LNMO do not change much during charge–discharge cycling, whereas the R values for the bare LNMO increases sharply. This strongly suggests that the Al_2O_3 ALD coatings suppress the side reactions successfully during continuous charge–discharge cycling.

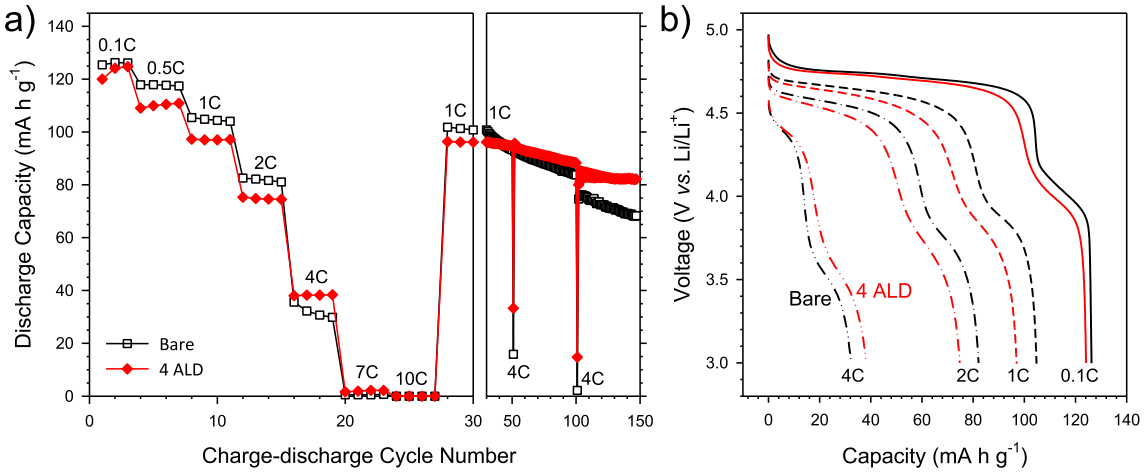

Fig. 3. a) Variation in the discharge capacities *vs.* charge–discharge cycle number and b) discharge voltage profiles for bare and Al_2O_3 ALD coated (using 4 ALD cycles) LNMO electrodes at different C-rates between 3.0 and 5.0 V.

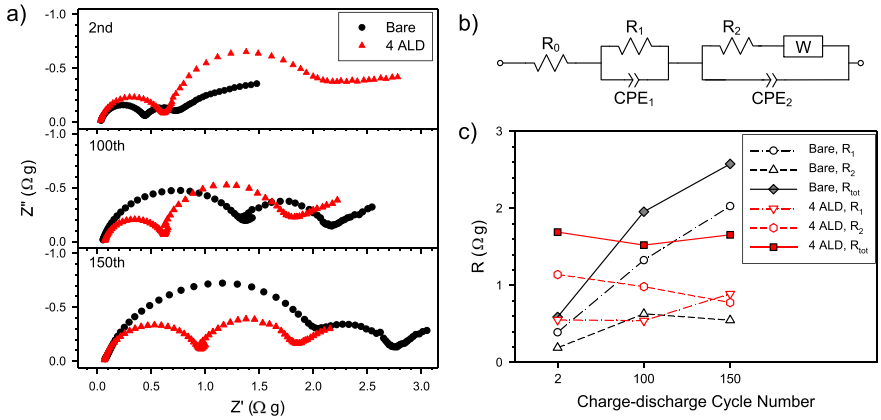

Fig. 4. EIS results for the bare and Al_2O_3-coated (using 4 ALD cycles) LNMO electrodes: a) Nyquist plots at different numbers of charge–discharge cycles, b) equivalent circuit model for fitting the EIS data in (a), and c) resistance values obtained from the EIS data in (a) using the model in (b).

The severe side reaction of LNMO at high operating voltage also leads to negative effects related to self-discharge [12]. Fig. 5 compares the results of self-discharge of bare and Al_2O_3 ALD coated (using 4 ALD cycles) LNMO. Fig. 5a and b shows the discharge voltage curves measured after the LNMO/Li cells were fully charged to 5 V (*vs.* Li/Li^+) and kept at 30 °C for various lengths of time. It is evident that the discharge capacities of the bare LNMO decrease significantly as the storage time increases whereas the Al_2O_3 ALD coated LNMO do not lose much capacity. The lowered discharge capacity after storage reflects the fact that the charged LNMO could self-discharge *via* the reaction [12].

$$Ni_{0.5}Mn_{1.5}O_4 + x\ Li^+ + \text{electrolyte} \rightarrow Li_xNi_{0.5}Mn_{1.5}O_4 + x\ \text{electrolyte}^+. \quad (1)$$

The lithiation of fully charged LNMO by self-discharge is also confirmed by the *ex-situ* XRD results shown in Fig. 5c. The smaller negative shift of the peaks associated with the Al_2O_3 ALD coated LNMO compared to those of the bare LNMO directly indicates a smaller amount of inserted Li [7]. In other words, there was less self-discharge.

The degrees of the dissolution of transition metals in bare and Al_2O_3-coated LNMO were also compared using ICPOES, as shown in Fig. 6. The overall amount of dissolved transition metal was obtained by collecting residuals not only from the used electrolytes and coin cell components, but also the cycled Li metal. The fully charged LNMO/Li cells kept at 30 °C for 7 days were used. The Al_2O_3 ALD coated LNMO exhibited significantly less dissolved transition metals. In particular, the amount of dissolved Mn recovered from the Al_2O_3 ALD coated LNMO cell is 6.6 times less than that recovered from the bare LNMO cell. Enhanced dissolution of Mn is related to the evolution of the soluble Mn^{2+} [36]. First, the disproportionation of Mn^{3+} can generate the Mn^{2+} [37]. Second, the severe side reaction in LNMO at high voltages also promotes the dissolution of Mn [12]. It has been reported that higher state of charge results in increased dissolution of Mn and Ni from LNMO [12]. At high voltages, anion oxidation can be accompanied by the reduction of Mn^{4+} to Mn^{3+}, which in turn leads to disproportionation and the generation of soluble Mn^{2+} [36]. Alternatively, the severe side reaction at high voltage is also known to produce more HF, which likely promotes the dissolution of transition metals [12,36].

From the extensive comparative analyses of coulombic efficiency, cycle performance, rate capability, EIS spectra, self-discharge behavior, and transition-metal dissolution measurements, it was confirmed that the Al_2O_3 ALD coating significantly suppressed the undesirable side reaction at LNMO surfaces. To understand the aforementioned behaviors in-depth, surface analyses were carried out. Fig. 7 shows the surface morphologies of bare and Al_2O_3 ALD coated (using 4 ALD cycles) LNMO electrodes

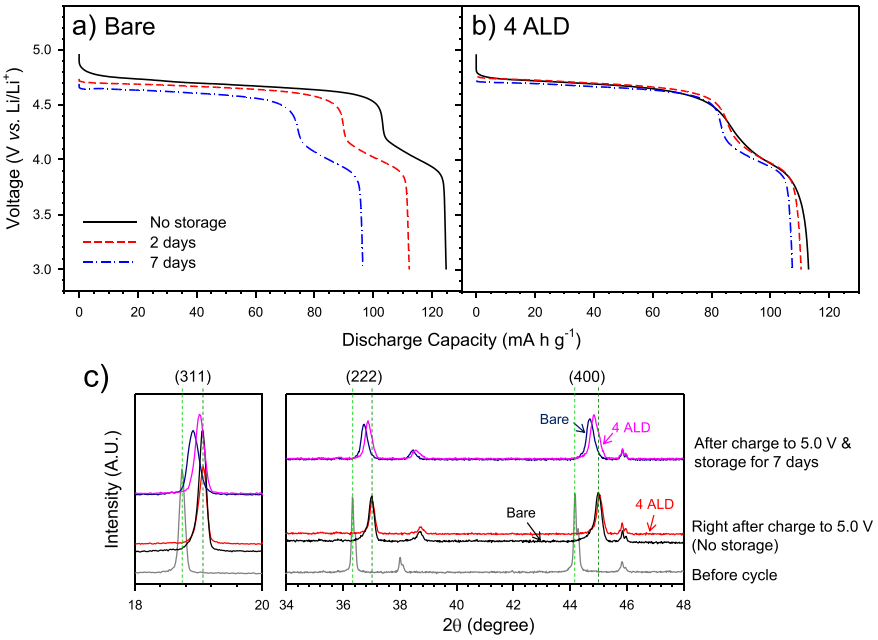

Fig. 5. Results of the self-discharge tests of bare and Al_2O_3-coated LNMO (using 4 ALD cycles) electrodes. Discharge voltage profiles of a) bare and b) Al_2O_3 ALD coated LNMO electrodes after the LNMO/Li cells were fully charged to 5 V at 0.1C and subsequently kept at 30 °C for different times. c) Corresponding *ex-situ* XRD results of the LNMO electrodes.

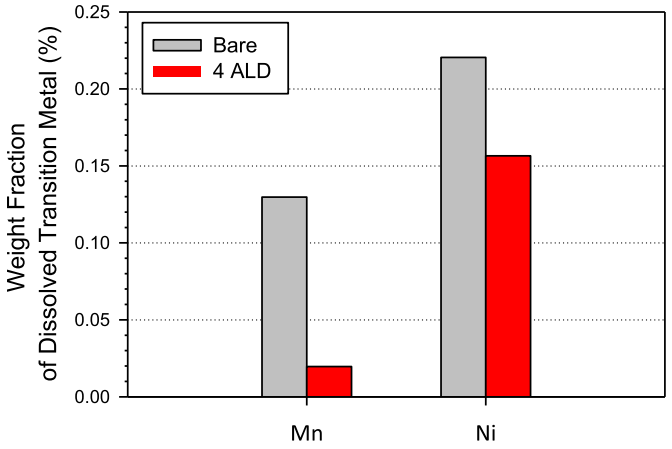

Fig. 6. Weight fraction of dissolved transition metals from the bare and Al_2O_3 ALD coated (4 ALD cycles) LNMO electrodes after the LNMO/Li cells were fully charged to 5 V at 0.1C and subsequently kept at 30 °C for 1 week.

before and after charge–discharge cycling. The pristine electrodes (Fig. 7a and c) have similar morphologies. After charge–discharge cycling, however, the surfaces of the electrodes look quite different. The bare LNMO electrode exhibits smooth surfaces, indicating a thick SEI layer was deposited. In contrast, the surface morphology of the Al_2O_3 ALD coated LNMO electrode does not change significantly. This suggests that the SEI layer on the Al_2O_3 ALD coated LNMO is much thinner than that on the bare LNMO, which in turn reflects a smaller degree of side reaction.

In order to collect in-depth information about the SEI layers, *ex-situ* XPS signals of for the C 1s, O 1s, F 1s, and Al 2p were collected for bare and Al_2O_3 ALD coated (using 4 ALD cycles) LNMO electrodes both before and after 50 charge–discharge cycles at 30 °C, as shown in Fig. 8. The peak assignments and deconvolution method were based on previous reports [24,38,39]. Comparing the signals after the 50 charge–discharge cycles, four features are notable. First, the relative intensity of the C–C peak at 285.0 eV in Fig. 8a is smaller for the bare LNMO electrode than the Al_2O_3 ALD coated LNMO electrode, which supports the assessment that there was a thicker SEI layer on the bare LNMO electrode. This behavior also agrees with the smaller intensity of the O 1s peak from $Ni^{(II)}O$ at 530.3 eV for the bare LNMO after charge–discharge cycling compared to the Al_2O_3 ALD coated LNMO, as shown in Fig. 8b. Second, much higher intensities related to organic species, including alkyl carbonates and Li_2CO_3, as well as inorganic species, such as $LiPF_xO_y$, are observed for the bare LNMO electrode compared to the Al_2O_3 ALD coated LNMO electrode, as indicated by the arrows in Fig. 8a and b. Third, a much higher intensity of the LiF peak at 685.6 eV is observed for the Al_2O_3 ALD coated LNMO compared to the bare LNMO, as shown in Fig. 8c. This behavior can be interpreted as the result of much thinner organic SEI components on the Al_2O_3 ALD coated LNMO electrode than on the bare LNMO electrode. However, a definite explanation is prohibited because the contribution of AlF_3 or AlO_xF_y may be superimposed on the LiF peak. Fourth, the Al 2p peak of the Al_2O_3 ALD coated LNMO shown in Fig. 8d becomes broadened and positively shifted after charge–discharge cycling. This result is a direct evidence of fluorination of the Al_2O_3 ALD coating layer by HF upon repeated charge–discharge cycles. The final composition of the Al_2O_3 ALD coating is somewhere in between Al_2O_3 and AlF_3. The chemically or electrochemically driven transformation of Al_2O_3 into AlO_xF_y should be accompanied by microstructural changes as well. Assuming the specific density of AlF_3 is ~3.0 g cm^{-3}, based on the crystallographic data for AlF_3 (JCPDS no. 43–0435: 2.82 g cm^{-3}, no. 44–0231: 3.13 g cm^{-3}, no. 47–1659: 3.02 g cm^{-3}) and considering the specific density of amorphous Al_2O_3 (~3.0 g cm^{-3}), the volume change produced by complete fluorination of Al_2O_3 to $2AlF_3$ is.

$$\frac{(2 \times \text{molar volume of } AlF_3) - \text{molar volume of } Al_2O_3}{\text{molar volume of } Al_2O_3} \times 100 = 64\% \quad (2)$$

which is comparable to the values obtained when the conversion-type transition metal oxides react with Li [40]. In this regard, the

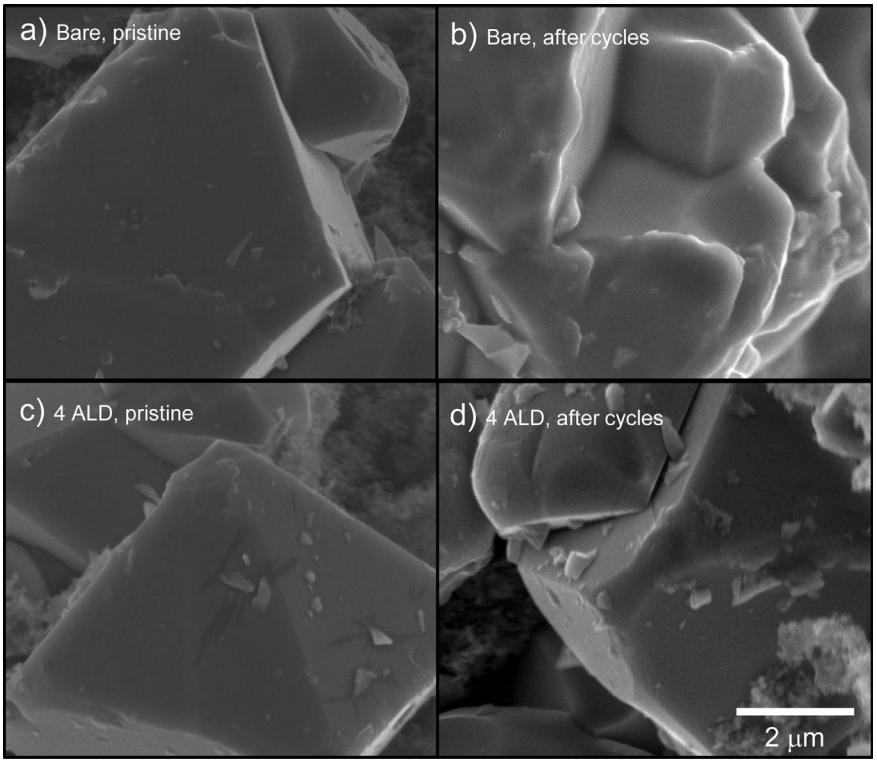

Fig. 7. FESEM images of bare and Al_2O_3-coated (4 ALD cycles) LNMO electrodes before and after 50 charge–discharge cycles.

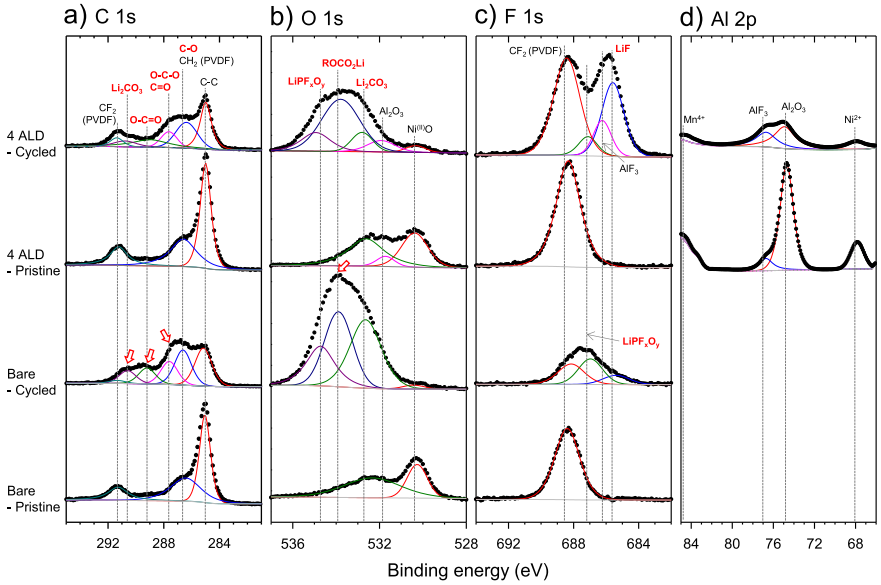

Fig. 8. *Ex-situ* XPS results of bare and Al_2O_3 ALD coated LNMO electrodes before and after 50 charge–discharge cycles. The signals for C 1s, O 1s, F 1s, and Al 2p are shown in (a), (b), (c), and (d), respectively.

possibility of cracks developing in the ALD coating layer during fluorination is not surprising. The microstructural changes induced by fluorination thus can lead to an increased rate of Li^+ ion transport, and consequently account for the dramatic increase in capacity during the initial charge–discharge cycles shown in Fig. 2c. However, the microstructural change in the ALD coating layer is not desirable in terms of conformality of the protective coatings. In this regard, further improvement of electrochemical performance of LNMO is believed to be possible by directly coating with AlF_3 by ALD.

Fig. 9 shows the depth profiles of cationic fragments obtained by *ex-situ* TOFSIMS experiments for the bare and Al_2O_3-coated LNMO electrodes after 50 charge–discharge cycles at 30 °C. The LiF^+ signals suggest that the Al_2O_3 ALD coated LNMO electrode is coated with slightly thinner F-bearing SEI species than the bare LNMO electrode. The CH_3^+ signals, which represent the organic SEI components, however, demonstrates the huge impact of the Al_2O_3 ALD coating. The etching time at which the intensity decreases to half of its original is 7.4 and 2.5 s for the bare LNMO electrode and the Al_2O_3 ALD coated LNMO electrode, respectively. This clearly

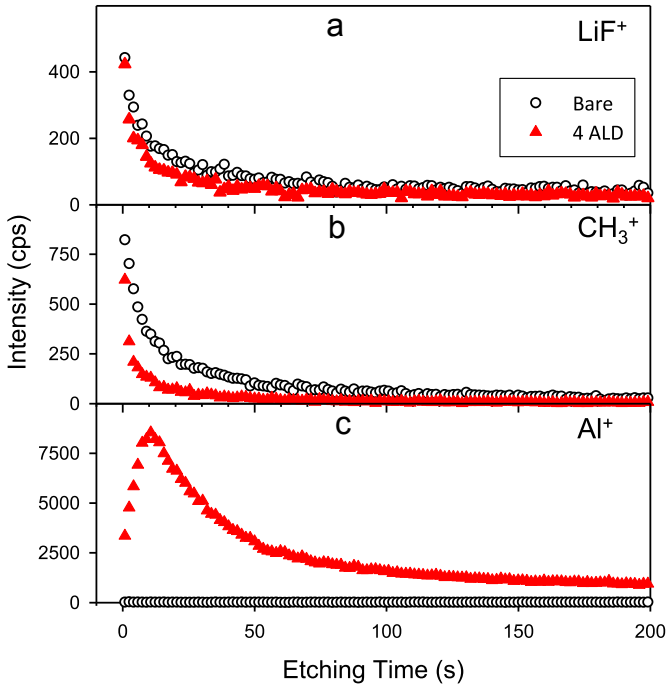

Fig. 9. *Ex-situ* TOFSIMS depth profiles of bare and Al_2O_3 ALD coated LNMO electrodes after 50 charge–discharge cycles for a) LiF^+, b) CH_3^+, and c) Al^+.

indicates a much thinner organic SEI component on the Al_2O_3 ALD coated LNMO than on the bare LNMO, which is nicely supported by the *ex-situ* XPS results in Fig. 8.

Based on the *ex-situ* surface analyses by XPS and TOFSIMS, a schematic diagram representing the SEI layers on bare and Al_2O_3 ALD coated LNMO particles after charge–discharge cycles was constructed; this is shown in Fig. 10. Compared to the bare LNMO particles, the Al_2O_3 ALD coated LNMO particles have much thinner SEI layers and the amount of organic species is lower. The Al_2O_3 ALD layer also became fluorinated.

Finally, full cells of LNMO/$Li_4Ti_5O_{12}$ incorporating bare and Al_2O_3 ALD coated LNMO were cycled between 2.00 and 3.45 V at 0.5C at 30 °C, as shown in Fig. 11. The full cell with the Al_2O_3 ALD coated LNMO appears to outperform the one with bare LNMO. The

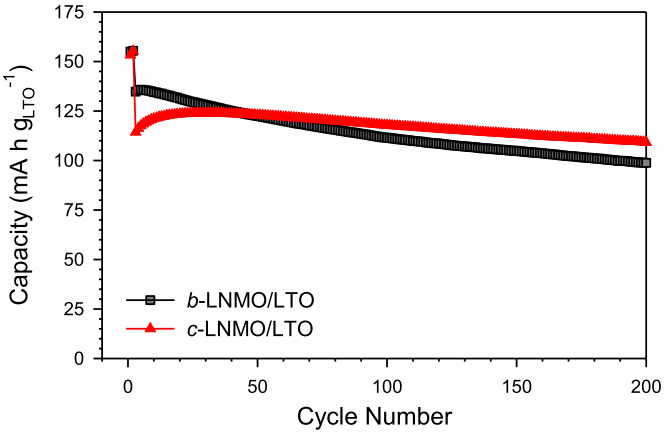

Fig. 11. Cycle performance of LNMO/LTO full cells cycled between 2.00 and 3.45 V at 0.5C at 30 °C. Bare (*b*) and Al_2O_3 ALD coated (*c*, 4 ALD cycles on powders) LNMO electrodes were used.

improved performance of the LNMO particles with the Al_2O_3 ALD coating can be explained by the enhanced stability of LNMO and the higher coulombic efficiency (or lower irreversible Li consumption), as demonstrated by the half-cell results.

4. Conclusions

Ultrathin (<1 nm) Al_2O_3 films were grown using ALD on LNMO particles. Significantly improved performance at 30 °C associated with the Al_2O_3 ALD coating was demonstrated not only in the coulombic efficiency, cycle retention, and rate capability, but also in the self-discharge behavior and the dissolution of transition metals. The combined *ex-situ* surface analyses using XPS and TOFSIMS revealed that the SEI layer on the Al_2O_3 ALD coated LNMO was much thinner and contained fewer organic species than the layer on the bare LNMO. This difference is the result of suppression of the side reaction at high voltages. Also, fluorination of the Al_2O_3 ALD layer was confirmed, shedding light on strategies for further improvement. Finally, the full LNMO/LTO battery incorporating the Al_2O_3 ALD coated LNMO was demonstrated to outperform the one incorporating bare LNMO.

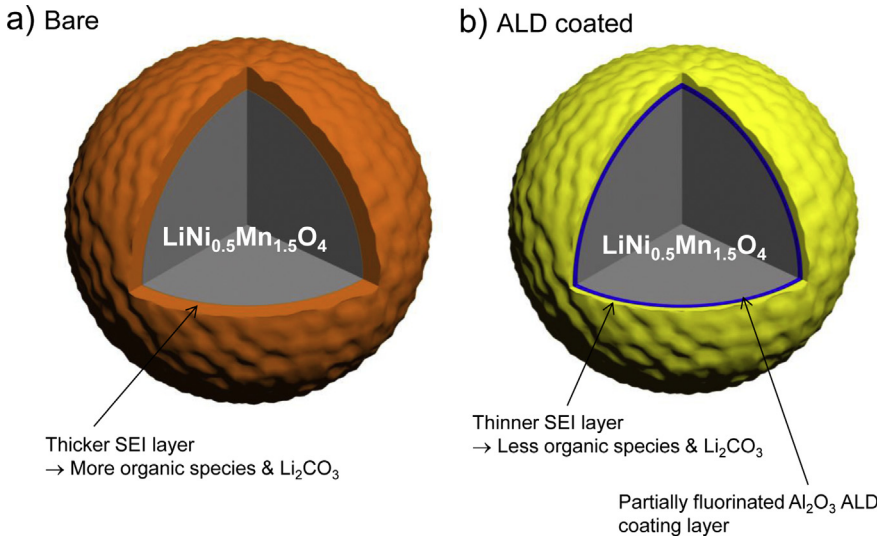

Fig. 10. Schematic diagram of a) bare and b) Al_2O_3 ALD coated LNMO electrodes after charge–discharge cycling, showing different features in the SEI layers.

Acknowledgment

This work was supported by LG Chem, by the Energy Efficiency & Resources Program of the Korea Institute of Energy Technology Evaluation and Planning (KETEP) grant funded by the Korea Government Ministry of Trade, Industry & Energy (No. 20112010100150), by the MSIP (Ministry of Science, ICT & Future Planning), Korea, under the C-ITRC (Convergence Information Technology Research Center) support program (NIPA-2014-H0301-14-1013) supervised by the NIPA (National IT Industry Promotion Agency), and by the Future Strategic Fund (1.130019.01) of UNIST (Ulsan National Institute of Science and Technology). Y. S. Jung appreciated Prof. Steven M. George at University of Colorado at Boulder for helping to build the rotary ALD reactor.

References

[1] M. Armand, J.-M. Tarascon, Nature 451 (2008) 652.
[2] J.B. Goodenough, Y. Kim, Chem. Mater. 22 (2010) 587.
[3] C.K. Chan, H. Peng, G. Liu, K. Mcllwrath, X.F. Zhang, R.A. Huggins, Y. Cui, Nat. Nanotech. 3 (2007) 31.
[4] X.L. Ji, K.T. Lee, L.F. Nazar, Nat. Mater. 8 (2009) 500.
[5] M.M. Thackeray, S.H. Kang, C.S. Johnson, J.T. Vaughey, R. Benedek, S.A. Hackney, J. Mater. Chem. 17 (2007) 3053.
[6] Q. Zhong, A. Bonakdarpour, M. Zhang, Y. Gao, J.R. Dahn, J. Electrochem. Soc. 144 (1997) 205.
[7] J.H. Kim, S.T. Myung, C.S. Yoon, S.G. Kang, Y.K. Sun, Chem. Mater. 16 (2004) 906.
[8] A. Kraytsberg, Y. Ein-Eli, Adv. Energy Mater. 2 (2012) 922.
[9] A. Manthiram, K. Chemelewski, E.-S. Lee, Energy Environ. Sci. 7 (2014) 1339.
[10] J. Xiao, X. Chen, P.V. Sushko, M.L. Sushko, L. Kovarik, J. Feng, Z. Deng, J. Zheng, G.L. Graff, Z. Nie, D. Choi, J. Liu, J.-G. Zhang, M.S. Whittingham, Adv. Mater. 24 (2012) 2109.
[11] T. Yoon, D. Kim, K.H. Park, H. Park, S. Jurng, J. Jang, J.H. Ryu, J.J. Kim, S.M. Oh, J. Electrochem. Soc. 161 (2014) A519.
[12] N.P.W. Pieczonka, Z. Liu, P. Lu, K.L. Olson, J. Moote, B.R. Powell, J.-H. Kim, J. Phys. Chem. C 117 (2013) 15947.
[13] S. Komaba, N. Kumagai, Y. Kataoka, Electrochim. Acta 47 (2002) 1229.
[14] N. MahootcheianAsl, J.-H. Kim, N.P.W. Pieczonka, Z. Liu, Y. Kim, Electrochem. Commun. 32 (2013) 1.
[15] X. Xiao, D. Ahn, Z. Liu, J.-H. Kim, P. Lu, Electrochem. Commun. 32 (2013) 31.
[16] M. Xu, D. Lu, A. Garsuch, B.L. Lucht, J. Electrochem. Soc. 159 (2012) A2130.
[17] Y.K. Sun, C.S. Yoon, I.H. Oh, Electrochim. Acta 48 (2003) 503.
[18] J.S. Park, X. Meng, J.W. Elam, S. Hao, C. Wolverton, C. Kim, J. Cabana, Chem. Mater. 26 (2014) 3128.
[19] S.M. George, Chem. Rev. 110 (2010) 111.
[20] Z. Chen, Y. Qin, K. Amine, Y.K. Sun, J. Mater. Chem. 20 (2010) 7606.
[21] Y.S. Jung, A.S. Cavanagh, A.C. Dillon, M.D. Groner, S.M. George, S.H. Lee, J. Electrochem. Soc. 157 (2010) A75.
[22] Y.S. Jung, A.S. Cavanagh, L.A. Riley, S.H. Kang, A.C. Dillon, M.D. Groner, S.M. George, S.H. Lee, Adv. Mater. 22 (2010) 2172.
[23] I.D. Scott, Y.S. Jung, A.S. Cavanagh, Y.F. An, A.C. Dillon, S.M. George, S.H. Lee, Nano Lett. 11 (2011) 414.
[24] Y.S. Jung, P. Lu, A.S. Cavanagh, C. Ban, G.H. Kim, S.H. Lee, S.M. George, S.J. Harris, A.C. Dillon, Adv. Energy Mater. 3 (2013) 213.
[25] Y.S. Jung, A.S. Cavanagh, L. Gedvilas, N.E. Widjonarko, I.D. Scott, S.H. Lee, G.H. Kim, S.M. George, A.C. Dillon, Adv. Energy Mater. 2 (2012) 1022.
[26] L.A. Riley, S. Van Ana, A.S. Cavanagh, Y. Yan, S.M. George, P. Liu, A.C. Dillon, S.H. Lee, J. Power Sources 196 (2011) 3317.
[27] J.W. Kim, J.J. Travis, E. Hu, K.-W. Nam, S.C. Kim, C.S. Kang, J.-H. Woo, X.-Q. Yang, S.M. George, K.H. Oh, S.-J. Cho, S.-H. Lee, J. Power Sources 254 (2014) 190.
[28] Y.S. Jung, A.S. Cavanagh, Y.F. Yan, S.M. George, A. Manthiram, J. Electrochem. Soc. 158 (2011) A1298.
[29] X. Xiao, P. Lu, D. Ahn, Adv. Mater. 23 (2011) 3911.
[30] L.A. Riley, A.S. Cavanagh, S.M. George, Y.S. Jung, Y. Yan, S.H. Lee, A.C. Dillon, ChemPhysChem 11 (2010) 2124.
[31] E. Kang, Y. Jung, A. Cavanagh, G. Kim, S. George, A. Dillon, J. Kim, J. Lee, Adv. Funct. Mater. 21 (2011) 2430.
[32] X. Fang, M. Ge, J. Rong, Y. Che, N. Arronyadet, X. Wang, Y. Liu, A. Zhang, C. Zhou, Energy Technol. 2 (2014) 133.
[33] M.D. Levi, D. Aurbach, J. Phys. Chem. B 101 (1997) 4630.
[34] M. Gaberscek, J. Moskon, B. Erjavec, R. Dominko, J. Jamnik, Electrochem. Solid State Lett. 11 (2008) A170.
[35] A.J. Bard, L.R. Faulkner, Electrochemical Methods: Fundamentals and Applications, second ed., John Wiley & Sons, Inc., New York, 2001.
[36] N.-S. Choi, J.-T. Yeon, Y.-W. Lee, J.-G. Han, K.T. Lee, S.-S. Kim, Solid State Ionics 219 (2012) 41.
[37] R.J. Gummow, A. Dekock, M.M. Thackeray, Solid State Ionics 69 (1994) 59.
[38] A.K. Dua, V.C. George, R.P. Agarwala, Thin Solid Films 165 (1988) 163.
[39] A. Hess, E. Kemnitz, A. Lippitz, W.E.S. Unger, D.H. Menz, J. Catal. 148 (1994) 270.
[40] Y.S. Jung, S. Lee, D. Ahn, A.C. Dillon, S.H. Lee, J. Power Sources 188 (2009) 286.